Cell Reports
Physical Science

Article

A battery-free wireless keyboard

Graphical abstract

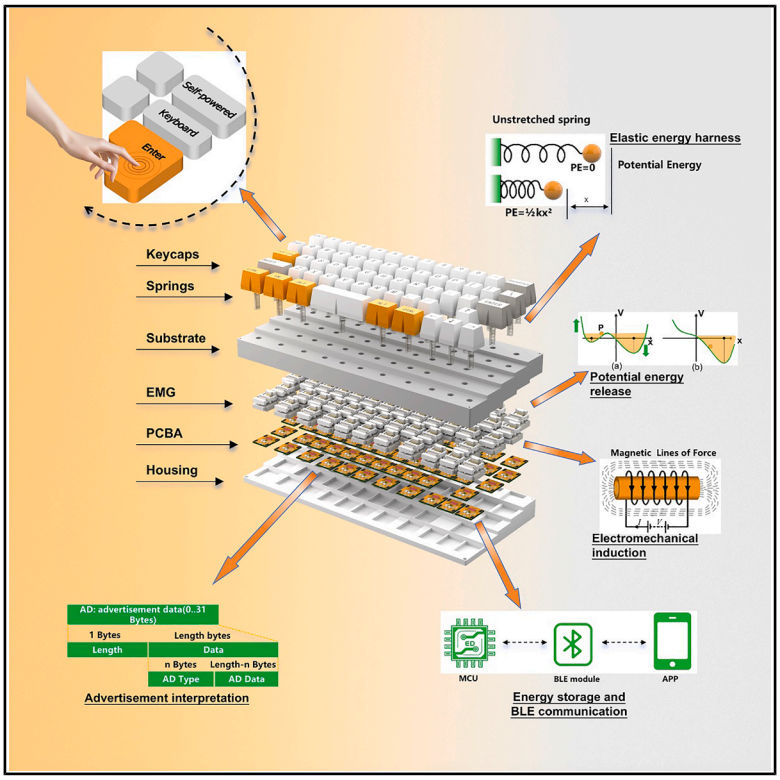

Highlights

- Battery-free wireless keyboard with full functionality and dense layouts
- Stable, user-invariant keystroke energy harvesting (≥45 μJ) via engineered dynamics
- Breakthrough in fingertip-powered interaction: command ~13.07 μJ, >16 m range, ~15 ms latency

Authors

Xin Li, Xinyuan Chuai, Yaoyi Li, ..., Congsi Wang, Guobiao Hu, Wei-Hsin Liao

Correspondence

lixin.phd@gmail.com (X.L.), guobiaohu@hkust-gz.edu.cn (G.H.), whliao@cuhk.edu.hk (W.-H.L.)

In brief

Li et al. present a fully functional, battery-free wireless keyboard that converts fingertip keystrokes into electrical energy via engineered dynamics. The system enables robust, user-invariant fingertip interaction with reliable service quality and real-time performance.

Li et al., 2025, Cell Reports Physical Science 6, 102972
December 17, 2025
https://doi.org/10.1016/j.xcrp.2025.102972

CellPress

Cell Reports
Physical Science

CellPress
OPEN ACCESS

Article

A battery-free wireless keyboard

Xin Li,[1,2,4,*] Xinyuan Chuai,[2,4] Yaoyi Li,[2,4] Yawei Wang,[3,4] Qitao Lu,[1] Yaozi Zheng,[3] Daxing Zhang,[2] Congsi Wang,[2] Guobiao Hu,[3,*] and Wei-Hsin Liao[1,5,*]

[1]Department of Mechanical and Automation Engineering, The Chinese University of Hong Kong, Hong Kong, China
[2]Guangzhou Institute of Technology, Xidian University, Guangzhou, China
[3]Thrust of Internet of Things, the Hong Kong University of Science and Technology (Guangzhou), Guangzhou, China
[4]These authors contributed equally
[5]Lead contact
*Correspondence: lixin.phd@gmail.com (X.L.), guobiaohu@hkust-gz.edu.cn (G.H.), whliao@cuhk.edu.hk (W.-H.L.)
https://doi.org/10.1016/j.xcrp.2025.102972

SUMMARY

Serving as a pivotal tool for human-computer interaction, the keyboard connects the physical and virtual worlds. Although wireless keyboards remove physical wires, they still face battery limitations. Here, we present a battery-free wireless keyboard that is powered by the energy harnessed from fingertip motion in keystrokes, completely getting rid of any physical constraints. The fingertip-motion energy harvester, based on specially engineered dynamics, consistently extracts at least 45 μJ from a single keystroke cycle, regardless of user habits, e.g., keystroke force, within a compact structure fully compatible with dense key layouts. A functional circuit establishes unidirectional communication with the computer, transmitting commands while maintaining minimal power consumption of 13.07 μJ. In over 400 practical tests, the system achieved a 100% success rate, a wireless communication range exceeding 16 m, and a stable latency of about 15 ms. This work marks a breakthrough in self-sustained human-computer interaction technologies, offering a scalable, manufacturable platform.

INTRODUCTION

Computers have emerged as essential and powerful tools in contemporary society, integral to routine work and a primary conduit for accessing data from the Internet.[1–3] As an essential part of the computer system, the keyboard serves as the primary interface for inputting and managing information across a variety of applications, including data acquisition, financial administration, security authentication, and social engagement.[4–6] However, existing power solutions are becoming problematic. As more and more appliances emerge in our daily lives, users have to carry more chemical batteries that require frequent replacement or recharging or to manage tangled wires connected to a central power source.[7–9] Both the reliance on chemical batteries and the complications associated with disorganized cable connections are considered undesirable.[10,11] An ideal and somewhat science-fiction solution is to generate power where it is being used.[12–15]

For devices such as keyboards, we expect that they can efficiently harness the biomechanical energy generated by human activities,[16–21] thereby eliminating the need for energy storage and distribution. During keystroke activities, fingertips hitting the keyboard generate a certain amount of mechanical energy.[22] By converting this biomechanical energy into electricity, we can not only open up possibilities for a sustainable power source to develop a fully self-powered keyboard but also capture behavioral sensing information from the users.[23,24] In the past years, numerous attempts have been made to tap this source, leveraging a wide range of technologies, including piezoelectric transduction,[25–29] triboelectric nanogenerators,[30–36] and even hybrid harvesting combining multiple transductions.[37–39] Chen et al.[30] and Li et al.[31] presented triboelectric keyboard covers that could harness energy from keystroke motions for self-powered human-machine interactions. However, these covers can only detect keystrokes and convert them into voltage signals. Auxiliary signal-processing circuits powered by external sources are still required to interpret these keystrokes. Based on a similar concept, Wu et al.[32] developed a triboelectric keystroke that transforms stroking actions into analog electrical signals. Nevertheless, the issue persists. Despite the claimed self-sensing capabilities for detecting keystrokes and enabling specific human-machine authentication through machine learning algorithms, an external power supply is needed to process the analog signals. Similarly, Jeon et al.[33] and Yi et al.[34] also developed fabric-based triboelectric wearable keyboards for wireless interfacing applications. However, the energy harnessed from a single keystroke action in all trials was found to be insufficient to meet the power requirements. Yin et al.[35] proposed a triboelectric keyboard to realize self-power transmission and noncontact reception. Each key integrates a triboelectric nanogenerator, a coil, and an external capacitor to generate wireless oscillating signals. However, the receiving coils must be in close proximity to the keys and require a power supply. Wacharasindhu et al.[37] designed a hybrid electromagnetic-piezoelectric energy harvester to power computer keyboards. However, their findings indicated that the output power generated was minimal,

remaining within the micro-watt range. This limited output raises questions about the practical viability of their design, highlighting the need for further enhancements to improve efficiency and power generation capabilities. Wang et al.[38] developed a hybrid electromagnetic-triboelectric sensor and integrated it into a keyboard to detect mechanical triggering. However, it was unable to achieve full keyboard functionality using only the sensor they developed. In addition, Maharjan et al.[39] also developed a hybrid keyboard that could generate up to 7.04 mW from the electromagnetic unit and 1.8 mW from the triboelectric unit embedded within a single key. However, experimental results showed that the harvested energy relies heavily on the speed of the keystrokes. Furthermore, while this design has been validated for powering a temperature sensor, its practical application in harvesting energy from keyboard actions remains unexplored and undescribed.

In the industries, Bai et al.[40] and some commercial companies, such as Logitech, have envisioned and even developed wireless keyboards powered solely by solar photovoltaic cells with the assistance of capacitors or rechargeable batteries.[41] However, due to the limited power outputs, such schemes cannot satisfy the power demands and have sacrificed service quality.[42] Therefore, such designs made a compromise by reducing the frequency of battery replacements instead of delivering a truly battery-free wireless keyboard. The above limitation arises from the fact that both the solar power solution and the previously mentioned keystroke-motion-driven approach are constrained by conversion efficiency, resulting in restricted power outputs. As a result, none of them can offer an absolutely stable energy solution for the keyboard. Since keyboards must be highly reliable and provide low latency in human-computer interactive processes,[43] the abovementioned unstable power solutions will significantly deteriorate the service quality and affect user experience.

By leveraging a cross-disciplinary design approach, this paper introduces a truly battery-free wireless keyboard with full features. The design concept is illustrated in Figure 1A. Through a highly integrated design of the mechanical structure, its nonlinear dynamics, and an ultra-low power consumption circuit, the proposed keyboard marks the first instance to achieve fully self-powered functionality. In response to a single keystroke, because of the intricately engineered hysteresis mechanism to release stable potential energy and the delicately designed abrupt magnetic-field-flipping behavior in a monostable structure, each key button can generate sufficient electrical energy to supply the auxiliary circuitry, enabling one-way communication with the computer.

Figure 1B shows the exploded view of the design keyboard. It comprises many components, especially the electromechanical generators (EMGs) and the printed circuit board (PCB) assembly (PCBA). Figures 1C and 1D briefly elucidate how electrical energy is harnessed from keystrokes by the keyboard. The entire process involves multiple stages of energy conversion, transitioning from biomechanical energy to elastic potential energy, then to magnetic energy, and finally to electrical energy. The functionalities of each component, the underlying working principles, and the design strategies employed to ensure the keyboard's robustness will be thoroughly explained from the perspectives of mechanical structure, dynamic mechanisms, and circuitry. In addition to assessing functionality and robustness, this work also presents the testing results concerning the interactive service quality. In various application scenarios, the developed battery-free wireless keyboard demonstrates a long communication range and low latency. A comprehensive comparison with other designs in the literature is provided in Table S3, addressing various aspects such as energy-harvesting methods, power-generation capabilities (including voltage, current, and power), and service quality metrics (communication range and latency). In general, this study, for the first time, demonstrates and validates the technical feasibility of developing an autonomous human-computer interaction device that harnesses opportunistic energy from real-time interaction activities. It is expected that the design approach presented in this work can be extended to develop more fancy, engaging, and, most importantly, battery-free human-computer interaction devices in the future.

RESULTS

Structural overview of an individual key button

Figure 2A illustrates the mechanical structure of a single key button, which is actually an EMG. It consists of multiple components from the top to the bottom, including a keycap, a buffering spring, a rotatable frame, a ferromagnetic bar wrapped with a coil, and a restoring spring. The buffering and restoring springs were iteratively tuned to ensure system reliability and consistent energy harvesting. The buffering spring accumulates energy during the press, whereas the restoring spring drives the reset motion and enables release-phase harvesting. Their stiffness and geometry were tailored to achieve a trade-off between sensitivity, robustness, and consistency across different users. A magnet is embedded within the rotatable frame. This subtle configuration can be more easily understood by examining the side cutaway view presented in Figure 2B.

At the core of the power-generating key button is the instantaneous magnetic pole-swapping mechanism. Under the combined influence of the magnetic interactions and the spring forces, the key button forms a monostable state with the equilibrium state, as depicted in Figure 2B-ii. In this state, the bottom of the rotatable frame maintains contact with the ferromagnetic bar. The key button can be toggled to the bottom (Figure 2B-ii) by applying light force with a fingertip. In this state, the top of the rotatable frame comes into contact with the ferromagnetic bar, limiting any further movement of the keystroke. Note that the head of the rotatable frame has a trench slot (refer to Figure 2B-i for a detailed view) specifically designed to restrict its rotation angle. The maximum rotatable angle range is constrained to $[-\theta_s, \theta_s]$.

The engineered dynamic feature of this switch facilitates and ensures a predetermined stable switching action, even at ultra-low-frequency excitation or under extremely slow actuation, such as quasi-static toggling. During the designed switching process, the magnetic flux through the coil undergoes an instantaneous reversal from positive to negative due to rapid changes in magnetic poles. Such a rapid magnetic flux reversal induces a pulsed electromotive force in the coil. The generated

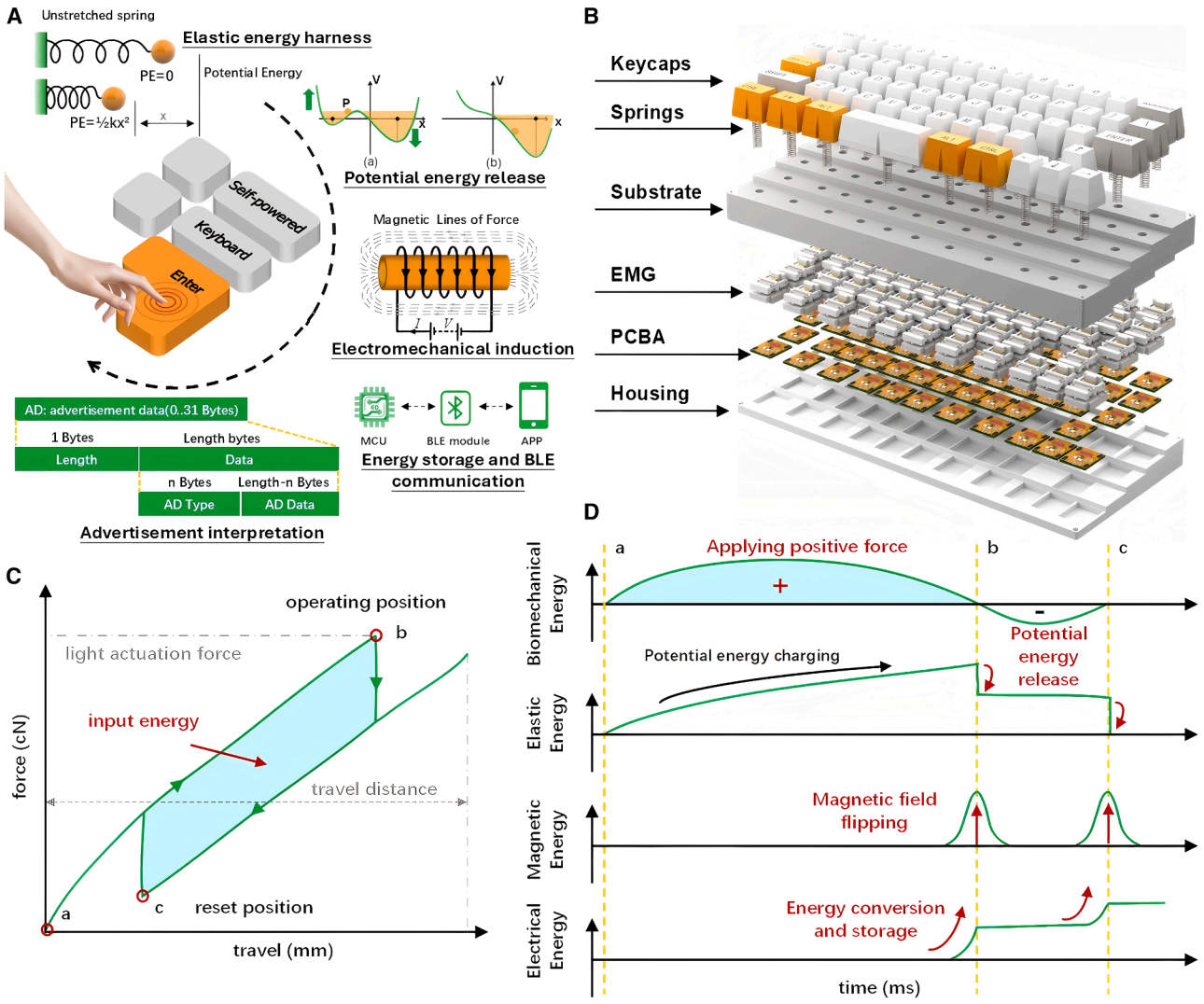

Figure 1. Illustration of the concept of the battery-free wireless keyboard

(A) The working logic of the keyboard. Subjected to a keystroke, the fingertip kinetic energy is converted into the potential energy stored in the key button. By leveraging a magnetic-field-flipping design, mechanical potential energy is converted into magnetic energy and then electrical energy via electromagnetic induction. A tailored low-power circuitry is designed to collect and store energy, which is subsequently utilized to operate a Bluetooth Low Energy (BLE) module for communication with the computer, enabling the transmission of keystroke commands. The computer captures the transmitted packets from the keyboard, decodes the information, and displays corresponding key symbols on the screen.

(B) The exploded view of the keyboard: it consists of keycaps, buffer springs, a substrate layer, electromechanical generators (EMGs), printed circuit board assembly (PCBA), and the housing.

(C) The intricately engineered hysteresis mechanism of the mechanical harvester in the key button to enable stable energy harvesting. Note: the unit "cN" (centinewton) of the *y* axis is commonly used in commercial keyboard specifications to describe key actuation force. It is defined as 1 cN = 0.01 N.

(D) Relationships between the applied fingertip forces, the key button movement, the produced voltage, and the harnessed energy.

electrical energy will be collected, stored, and utilized to power the keyboard's communication function. A detailed explanation of the functional circuit design will be provided in a subsequent section.

Finger-motion energy-harvesting process

During the functioning of the power-generating switch, electrical energy can be harvested from keystrokes. When a keycap is pressed, the buffering spring is compressed and deformed, storing a specific quantity of potential energy. Once the applied force exceeds the magnetic attraction between the magnet and the ferromagnetic bar, the stored energy is released in a burst mode, toggling the rotatable frame downward. From the perspective of power generation, it is well known that the electromotive force generated by electromagnetic induction is proportional to the magnetic flux change rate. In other words, the more often and faster the magnetic flux changes, the higher the voltage is generated. Therefore, the designed burst mode is

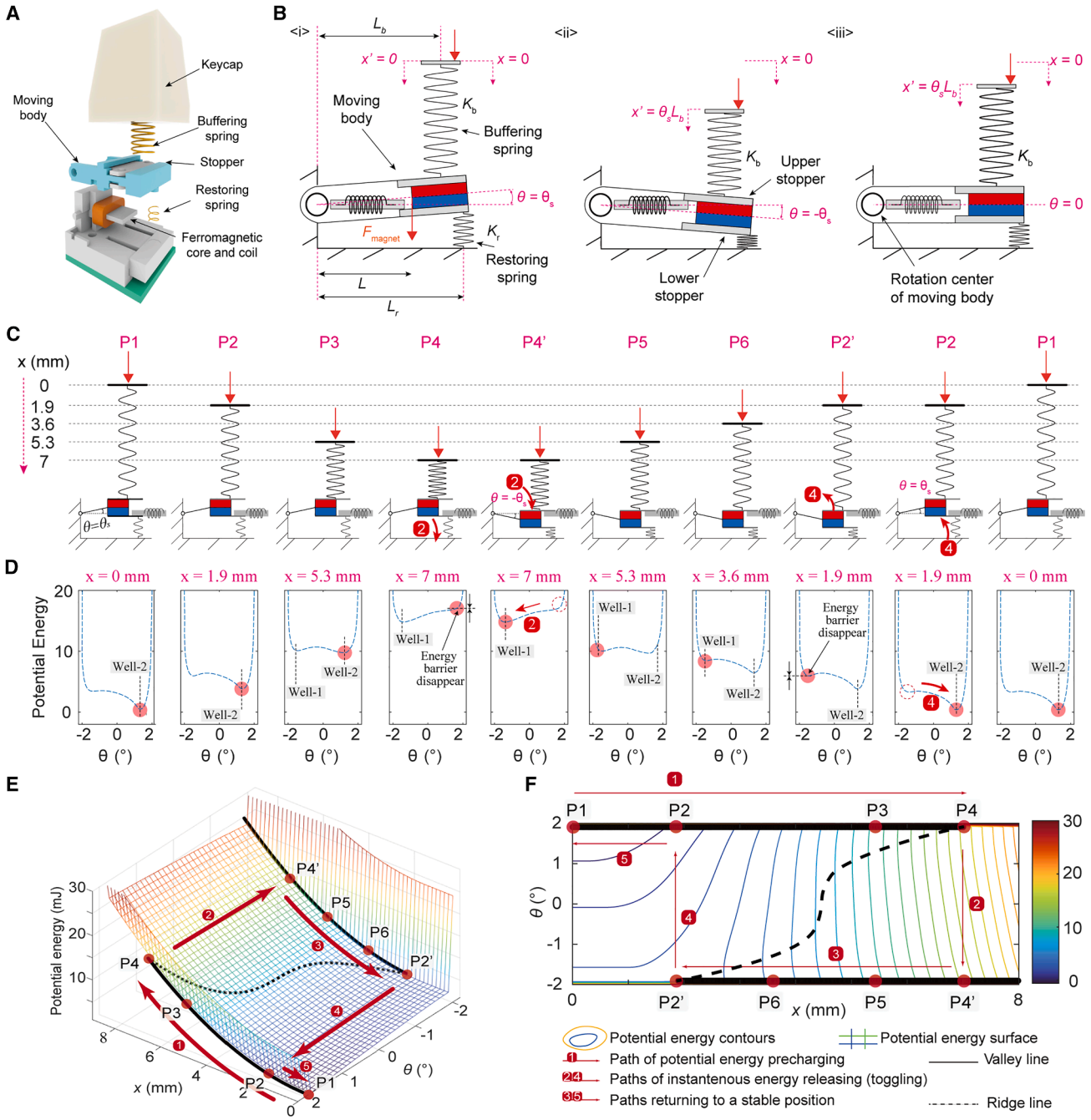

Figure 2. Structure and operation mechanism of a single key button

(A) The exploded view of a key button that comprises a keycap, a buffering spring, a rotatable frame, a ferromagnetic bar encircled by a coil, and a restoring spring.

(B) Relative positions of mechanical components during the switch toggling action. (i) The toggled-up state, (ii) the toggled-down state, and (iii) the intermediate state.

(C) Different states of the switch throughout one cycle of toggling. P4-P4′ and P2′-P2 are two critical phases during which potential energy autonomously releases and energy harvesting could be conducted without affecting the keystroke action.

(D) Corresponding potential energy profiles during the toggling cycle.

(E) 3D potential energy evolution during the toggling cycle. The solid black lines represent the valleys, and the dashed curve represents the ridge. The red arrows indicate the process-proceeding direction.

(F) The corresponding 2D contour plot.

intended to maximize the efficiency of electromechanical energy conversion.

Figure 2C illustrates the entire process of a single keystroke cycle, demonstrating how the finger-motion energy is captured and converted into electricity by the power-generating switch. From left to right, the fingertip first makes contact with the keycap, applies force, and finally moves away, releasing the exerted force. Due to the restoring spring, the switch reverts to its initial position, P1, as the force exerted by the fingertip is removed. For the different positions (P1–P6) presented in Figure 2C, Figure 2D presents the corresponding potential energy profile of the switch. In the initial phases (P1–P3), as the fingertip presses, the buffer spring compresses, accumulating potential energy. This process can be mathematically described by the elevation of potential well 2, as depicted across the first three insets of Figure 2D. Meanwhile, the switch remains in the toggled-up position due to the magnetic attraction between the magnet in the rotatable frame and the ferromagnetic bar. It is worth noting that the switch is in a monostable state when no fingertip force is applied. As the fingertip presses the buffer spring down, the dynamics of the system change, transitioning to a bistable system with a second potential well formed on the left-hand side in the inset P3 in Figure 2D.

When the fingertip further presses down to a critical position (P4), i.e., the potential energy stored in the buffer spring reaches a maximum threshold, the magnetic attraction force can no longer sustain the switch in the toggled-up position, resulting in a rapid transition to the toggled-down position. An analysis of the potential energy profile reveals that this transition occurs due to the disappearance of the potential barrier separating the two potential wells, prompting the system to gravitate toward potential well 1, as indicated by the red arrow in the inset P4′ in Figure 2D. In this process (P4-P4′), the potential energy autonomously releases for the first time, allowing for a portion of it to be converted and harvested. Due to the trench slot incorporated in the head of the rotatable frame, the switch cannot be toggled down any further.

The insets P5–P6 in Figure 2D present the force-release process. As the fingertip slowly moves away, the buffer spring first rebounds up. However, the switch remains in the toggled-down position due to the magnetic attraction. Once the fingertip retracts up to a critical height (P2′) and the buffer spring is released to an extent, failing to generate sufficient force to counteract the restoring spring's force, the restoring spring will rebound, transitioning the switch back to the toggled-up state (the right-hand side P2 in Figure 2D). P2′-P2 represents the second process within a single keystroke cycle during which the system autonomously releases potential energy. This enables a second-time energy conversion and collection. Similar to the P4-P4′ process, the P2′-P2 process is also accompanied by the disappearance of the potential barrier between two potential wells, inducing the system to gravitate from one potential well to another.

The 3D plot in Figure 2E elucidates the dynamics of the potential energy profile throughout a single keystroke cycle in more detail, from the initial contact of the fingertip with the keycap to its full retraction. The entire process can be analogized to a cyclical ascent and descent akin to the movement along a mountain slope. The solid bold lines indicate valley paths of the "mountain," and the dashed curve marks the ridge, which is the potential barrier. Without any external force, the system stabilizes at the foot corner of the mountain, as marked by P1 in Figure 2E. Given any disturbance, the system will finally return to the foot corner, where the potential energy is the lowest. In the initial phase, the significant elevation difference to the "mountain ridge" presents a challenge for crossing. The fingertip force propels the system to ascend the mountain via the left-hand valley path, leading to an elevation in potential energy. As the potential energy rises to the critical threshold, identified as P4, the ridge vanishes, which simplifies the crossing and enables the system to autonomously "slide" into the other valley path. This transition process releases potential energy spontaneously; thus, energy recovery can be conducted without obstructing the execution of the keystroke action. Following this transition, a descending process occurs, driven by the system's inclination to sustain low potential energy levels. Likewise, the descent will proceed along the valley trajectory until it attains the second critical position, P2, where the ridge vanishes again. The system will then slide back to the original valley path, ultimately returning to the foot corner of the mountain, thereby signifying the completion of a keystroke cycle. During the valley path transition process, potential energy is released spontaneously once more, allowing for a second-time energy recovery. A 2D contour in Figure 2F is also provided to enhance understanding from an aerial viewpoint.

Dynamics and energy output evaluation

The dynamics of the monostable key button are meticulously designed to maintain a consistent release of potential energy in response to keystrokes. Figures 3A and 3B illustrate the transient voltage and current responses of the power-generating key button, respectively. One keystroke cycle is completed quickly, within approximately 0.2 s. The response curves in both figures exhibit two sharp spikes that indicate power generation. These sharp spikes correspond to the previously mentioned potential energy release processes, each occurring within a time frame of several milliseconds. The power output is also influenced by the external load. Figure 3C displays the root mean square (RMS) power output of the key button under varying load resistance. A maximum power output of about 140 μW is obtained at 60 Ω, which aligns with the internal resistance characteristics of the key button as predicted by impedance-matching theory.

Figure 3D illustrates the force-displacement relationship measured in the experiment and obtained from the simulation. The result characterizes the mechanical behavior of the key button during the loading and unloading phases. The shaded region between the loading and unloading curves represents the hysteresis loop, which indicates energy "dissipation" in the loading-unloading cycle. The observed energy loss results from material damping, energy conversion, and other dissipative mechanisms. By integrating the shaded region, the total energy loss in one keystroke cycle is about 3.9 mJ. The previously observed variations in the potential energy profile, which facilitate the release of potential energy during the keystroke action, stem from the nonlinear characteristics of the magnetic force, as demonstrated in Figure 3E. In the absence of this nonlinear

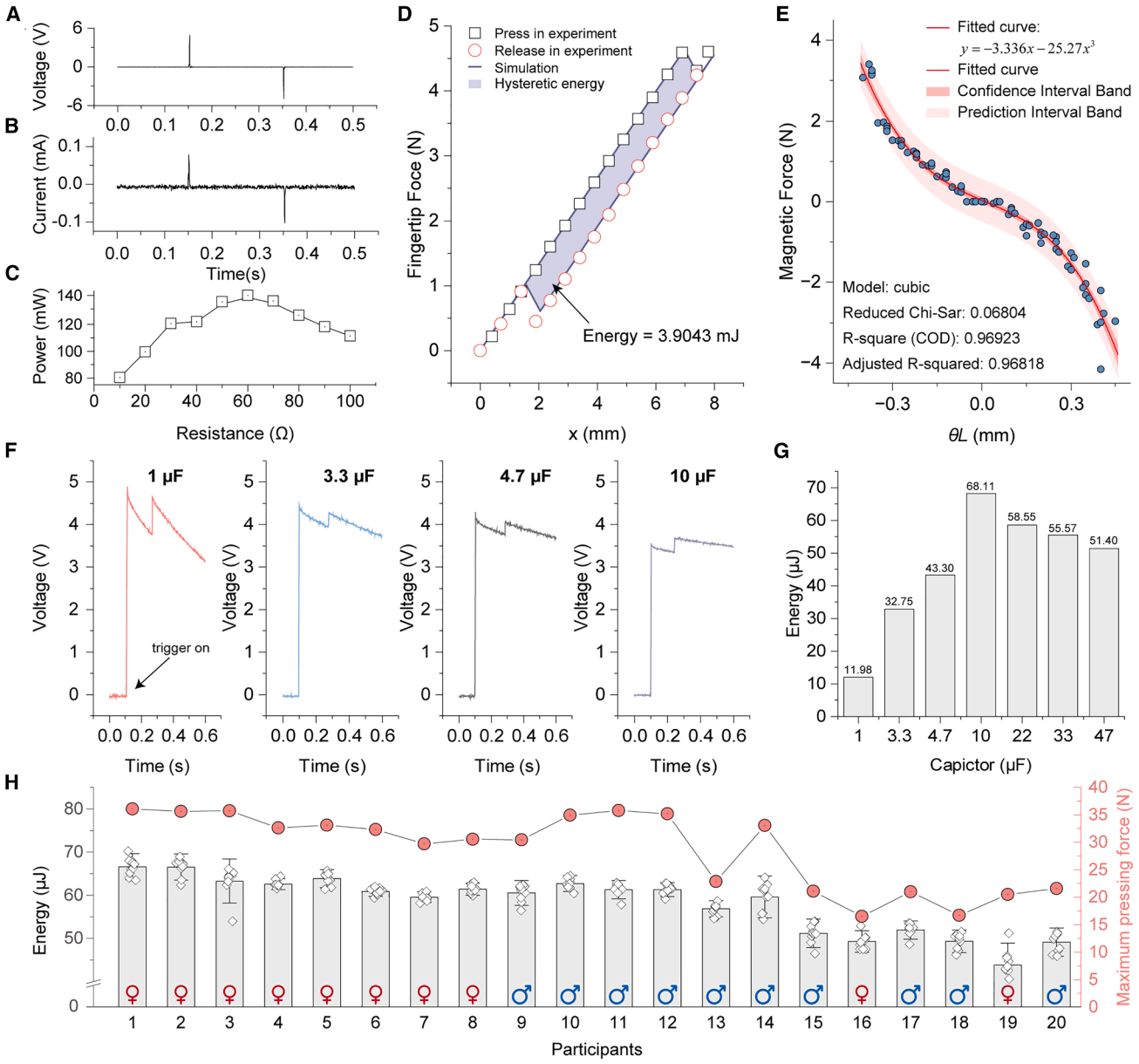

Figure 3. Performance evaluation of a single key button during a toggling cycle

(A) The open-circuit voltage produced by the switch during a keystroke cycle.

(B) The generated short-circuit current.

(C) The RMS power outputs versus load resistance.

(D) Force-displacement relationships obtained from experimental measurements and simulations. The force represents the reaction force experienced by the fingertip under the combined influence of magnetic interactions and buffer and restoring springs.

(E) The experimentally identified magnetic force and the fitting curve. The effects of the buffer and restoring spring forces are excluded in this experiment.

(F) Results of the capacitor charging test.

(G) Collectible energy using different capacitors.

(H) Harvested energy from different users. This test was conducted with 20 participants: 10 females and 10 males.

force, the hysteresis phenomenon illustrated in Figure 3D would not manifest.

This button is designed to eliminate the reliance on batteries. However, a capacitor remains essential for the temporary collection and storage of energy. As determined by the impedance-matching principle, choosing different capacitors results in varying quantities of energy being harvested. Figure 3F shows representative capacitor charging results. The voltage curve features two sharp rises corresponding to the press and release energy-harvesting events during a keystroke. Each event

(press/release) induces a burst of voltage across the coil, which charges the capacitor via the rectifier. The slight decline between the two peaks is due to inherent energy loss in non-ideal capacitors, such as leakage current and dielectric dissipation. This natural decay accounts for the small but noticeable voltage drop during the short interval between transitions. With the increase in capacitance, the saturation voltage decreases, since the harvestable energy is limited. Moreover, a small capacitor shows a relatively larger energy leakage and faster voltage drop. To ensure repeatability in evaluating the capacitor charging performance shown in Figure 3F, the keystroke was applied using a micro-positioning stage under quasi-static conditions, as illustrated in Figure S11. This setup allowed for slow and controlled actuation of the keycap, minimizing dynamic variability and isolating the energy-harvesting behavior. The maximum applied force during this process was approximately 4.8 N, which was sufficient to trigger the pole-swapping motion and enable both the press and release energy-harvesting events.

Figure 3G reveals the harvestable energy when utilizing different capacitors. Among the tested capacitors, a 10 μF capacitor delivers the largest energy of 68.11 μJ. To calculate the total energy harvested per keystroke, we consider the net increase in stored energy across both charging events, using the formula $E = C(V_{final}^2 - V_{initial}^2)/2$, where $V_{initial}$ is the baseline voltage before the keystroke (set to 0 in our case) and V_{final} is the peak voltage after the second charging event. This approach accounts for the cumulative energy harvested from both the press and release actions, while incorporating any loss between the two. Given that the total mechanical energy loss in one keystroke cycle is about 3.9 mJ, the overall energy conversion efficiency of the designed power-generating button is calculated to be around 1.75%. Although the overall energy conversion efficiency of the designed power-generating button may seem low at first glance, it is important to consider the complexity of the multiple-stage energy conversion process involved. Each stage—from biomechanical energy to elastic potential energy, then to magnetic energy, and finally to electrical energy—introduces inherent challenges and losses. The intricate nature of these conversions makes achieving higher efficiency extremely difficult.

To validate the robustness of the power-generating button from the energy perspective, a cohort of 20 volunteer participants, consisting of 10 females and 10 males aged between 20 and 45 years, was recruited for testing. The 20 participants were instructed to press the key button in the same manner they would utilize their keyboards. A data acquisition system measured and recorded the maximum fingertip force applied and the energy harnessed during their keystrokes. Figure 3H presents the post-processed results. Despite the apparent variation in energy output among participants, the results reflect natural differences in keystroke force and style. Users who applied stronger keystrokes induced faster pole-swapping motion and higher flux change rates, resulting in greater harvested energy. In contrast, lighter keystrokes produced lower output, but as long as the actuation exceeded the design threshold, the engineered mechanism ensured a minimum-speed transition and consistent baseline energy generation. As a result, the system reliably harvested at least ~45 μJ per keystroke across all users. It is worth noting that the keystroke force values reported in Figure 3H (16–36 N) appear significantly higher than those observed in the controlled experiment shown in Figure 3D (<5 N). This difference arises from the distinct testing methods and measurement conditions. In Figure 3D, the force-displacement relationship was obtained under quasi-static loading using a micro-positioning stage and a force gauge directly applied to the keycap, thereby excluding inertial and impact effects. In contrast, Figure 3H reflects real-world dynamic typing by human users, where the peak force was captured using a handheld force gauge. These higher measured values inherently include transient impacts, finger acceleration, and short contact durations, which result in elevated peak readings compared to the quasi-static case. This explains the apparent discrepancy and underscores the difference between idealized testing and practical user operation.

For the test and evaluation of a single key, one can refer to Video S1.

Functional circuit design and implementation

In addition to the mechanical structure of the power-generating button, the auxiliary circuitry must also be meticulously designed to minimize power consumption and enhance functional reliability. Figure 4A shows the circuitry schematic designed to realize one-way communication from the keyboard to the computer. The circuitry comprises a rectifier bridge for converting the alternating current (AC) output from the power-generating button into direct current (DC), a low-dropout regulator (LDO) to stabilize the DC output at 1.8 V to meet the power supply requirement of the following energy usage node, and a finite state machine (FSM) that controls a Bluetooth Low Energy (BLE) module to enable one-way communication from the keyboard to the computer at the expense of minimal power consumption. The FSM uses a 32 kHz resistor-capacitor (RC) oscillator rather than a crystal to simplify the circuit design and reduce cost. More importantly, RC oscillators typically consume less power than crystals. This is particularly beneficial in our application scenario, where the harnessed energy is severely constrained. The BLE module is compliant with Bluetooth 5, which allows for entering sleep mode when not in use to minimize energy usage during idle times. To facilitate the transmission of commands from the battery-free key button to a computer, a BLE beacon advertisement scanner was developed. The scanner establishes a communication link with the computer via a universal asynchronous receiver-transmitter (UART) interface. Each key on the keyboard is assigned a unique identifier within the advertisement packet it transmits. Upon capturing and decoding the BLE advertisement packet, the computer interprets the embedded identifier and inputs the corresponding key at the cursor's location on the screen.

Figure 4B illustrates how BLE advertising data flow from configuration memory, through FSM control, and are finally transmitted in a BLE-compliant packet structure over the 2.4 GHz frequency. The system uses a well-defined process, leveraging shared memory, advertising control settings, and FSM logic to manage packet transmission efficiently. The 4 KB static random-access memory (SRAM)-shared memory serves as a buffer for handling the advertising configuration and data

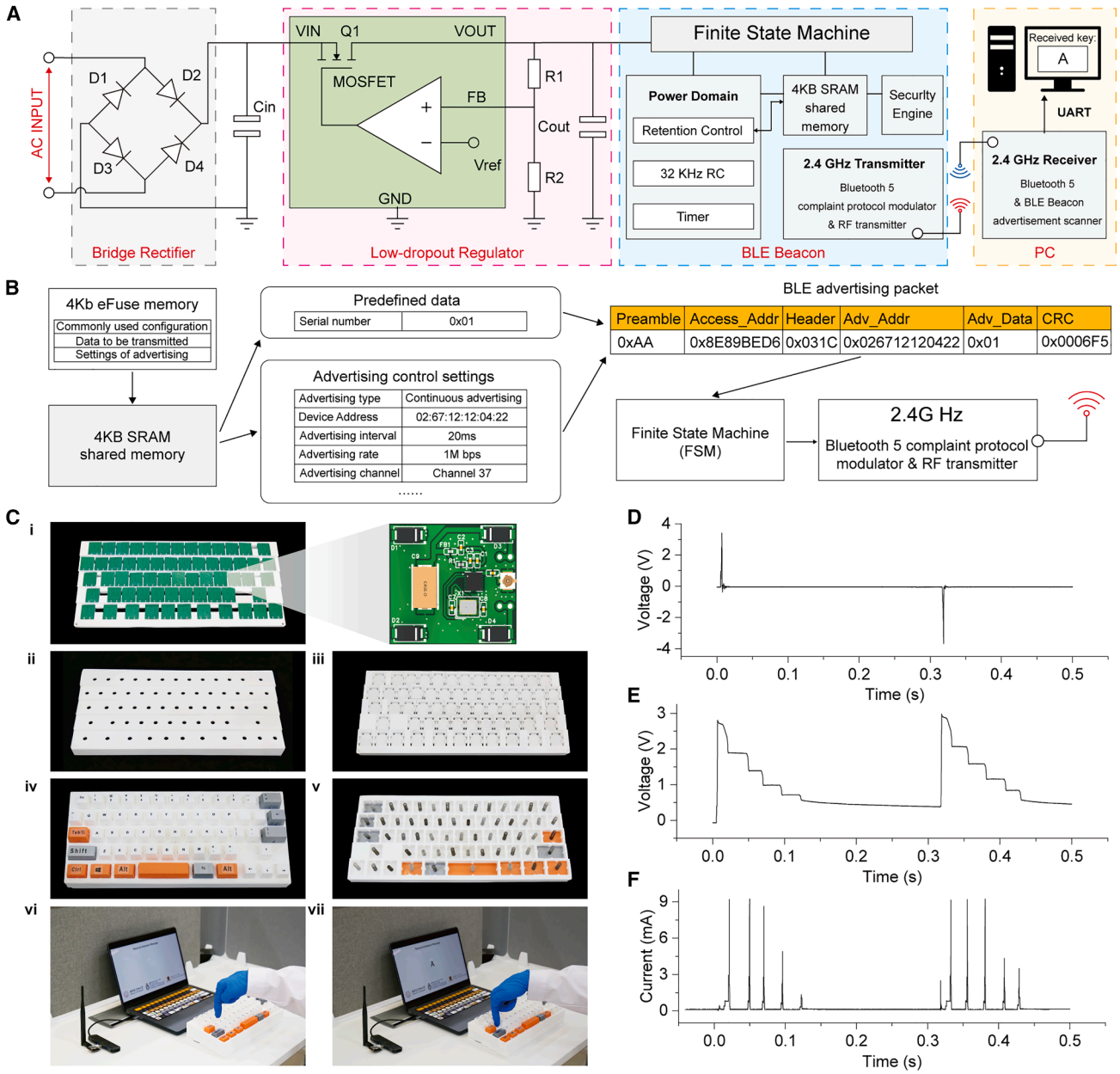

Figure 4. Auxiliary circuitry, keyboard implementation, and function verification

(A) Schematic of the functional circuitry consisting of a bridge for AC-DC conversion, a low-dropout regulator (LDO) to stabilize the DC output at 1.8 V, and a finite state machine (FSM) that governs a Bluetooth low energy (BLE) module to facilitate one-way communication from the designed keyboard to the computer.

(B) Architecture and process flow of BLE advertising, showing memory configuration, control settings, BLE advertising packet structure, and the transmission process using a Bluetooth 5-compliant RF transmitter.

(C) Implementation of the battery-free keyboard, illustrating the hierarchical structure from the bottom layer to the top layer. The circuitry is integrated within the bottom layer, with various components 3D printed in distinct colors for easy identification: red for the keyboard base, green for the PCB, white for the key switch, and other colors for the keycaps.

(D) The AC voltage response (i.e., the AC input in A) during a keystroke action.

(E) The rectified DC voltage in the storage capacitor (i.e., Cin in A).

(F) The current flowing into the LDO.

shared across the BLE stack. The key parameters for BLE advertising are specified: advertising type, continuous advertising; device address, 02:67:12:12:04:22 (unique identifier); advertising interval, 20 ms; advertising rate, 1 Mbps; and advertising channel, channel 37 (BLE-specific advertising channel). The structure of the BLE advertising packet consists of a preamble (0xAA) for

synchronization, an access address (0x8E89BED6) for identifying the packets, a header (0x031C) specifying the packet type and length, an advertising address (0x026712120422) for the device, application-specific advertising data (Adv_Data) that carry a per-key unique identifier (illustrated as 0x01 in Figure 4B), and a cyclic redundancy check (CRC) (0x0006F5) for error detection. For key differentiation, the FSM writes each button's unique key identifier into Adv_Data, while Adv_Addr (e.g., 0x026712120422) and header fields are used for source validation. The FSM controls packet creation and transmission, ensuring that BLE packets adhere to the defined protocol. The BLE advertising packet is transmitted using the Bluetooth 5 protocol at a frequency of 2.4 GHz via the radio-frequency (RF) transmitter. At the receiver, the BLE scanner relays the decoded advertising record to the host over UART without modifying Adv_Data. In the host, the program validates the source using Adv_Addr and required header fields, extracts the key identifier from Adv_Data, maps it to a character via a lookup table, and applies a 500 ms per-character temporal de-duplication window. The end-to-end flow is summarized in Figure S15.

The above describes how a single key button works. Based on this working principle, we built a fully functional keyboard. Figures 4C-i–4C-vii demonstrate the assembly process of the keyboard with a hierarchical structure from the bottom to the top layer. The circuitry for each key on the keyboard is independently constructed, with the components integrated within the base layer. To facilitate identification, various elements are fabricated using different materials in different colors: red for the keyboard base, green for the PCB, white for the key switches and alphabet keycaps, and other colors for other keycaps. Figures 4C-vi and 4C-vii demonstrate that once a user types the alphabet key "A" on the keyboard, the well-configured computer can detect and input the letter "A" on the screen. A recorded video of this test, along with a more complex assessment, is available in Video S1.

For the test shown in Figures 4C-vi and 4C-vii, Figures 4D–4F display the voltage and current responses in the circuitry during a single keystroke action. The voltage response in Figure 4D was measured from the power-generating button. The AC voltage signal contains two distinct sharp spikes: one positive spike and one negative spike, corresponding to the two energy-harvesting processes associated with the switch toggling down and up, respectively. Figure 4E shows the voltage across the storage capacitor, labeled Cin in the circuit schematic of Figure 4A. The stored energy, indicated by voltage, exhibited an increase twice during the keystroke action, echoing the two-phase energy-harvesting processes. The staircase-like voltage drops depicted in Figure 4E are caused by the energy usage of the FSM. Compared with the number of staircases, i.e., voltage drops, in Figure 4E, the same number of current spikes observed in Figure 4F confirms the functioning of the FSM. Video S2 can be referred to for the functionality demonstration of a single key.

Testing of the interactive quality of the keyboard

Leveraging the previously described cross-disciplinary design, a truly battery-free wireless keyboard has been developed and is ready for practical application. To evaluate its interactive performance, four application scenarios, as shown in Figures 5Ai–5Aiv, have been designed for testing: (1) a nearby scenario representing a normal working mode, (2) a far-distance scenario simulating the theater mode, (3) a cross-door scenario modeled after conference room conditions, and (4) a "noisy" scenario to assess performance in the presence of interference from multiple Bluetooth devices around, respectively. While the BLE protocol specifies a theoretical maximum communication range under ideal conditions, the actual transmission distance in our battery-free system is constrained by the available transmission power, which in turn depends on the energy harvested from each keystroke. In our tests, this energy typically ranged from 45 to 68 μJ, directly influencing the signal strength and range. As BLE devices support dynamic adjustment of transmission power based on available energy, the effective communication distance may vary in energy-limited scenarios. Therefore, we performed distance-dependent characterization to empirically validate that the harvested energy from a single keystroke is sufficient to sustain reliable BLE packet transmission under various practical conditions. This assessment demonstrates the real-world robustness and functionality of our self-powered keyboard.

A multi-channel oscilloscope was used to concurrently detect the voltage produced by the keyboard and the signal captured by the receiver. The results are presented in Figure 5B. Through the analysis of the detected signals, one can judge the success or failure of communication across various application scenarios while also quantifying communication latency. The results illustrate that in the four testing scenarios, the keyboard is capable of harvesting sufficient energy to transmit multiple packets, i.e., at least two, with a single keystroke. While the ample energy harvested enhances the robustness of the keyboard, it also introduces challenges in accurately identifying the key command. The transmission of multiple packets in response to a single keystroke excitation can lead to confusion, resulting in incorrect command interpretation. Fortunately, the intervals between the consecutive packets transmitted in a single keystroke cycle are at the millisecond level. A proficient typist can typically type between 40 and 60 words per min. Consider that an average English word is about 5 letters long, plus a space, which means a typical person can type between 200 and 300 letters (characters) per min, depending on their typing proficiency. In other words, the interval between keystrokes for an average person is about 0.2–0.3 s. Given the above information, an algorithm could be easily developed to differentiate between packets generated from a single keystroke and other keystrokes. Figure 5B also reveals that the duration from the initiation of the keystroke action to the reception of the corresponding key command is approximately 15 ms across all four scenarios, accounting for the first packet received. This suggests that communication latency remains relatively constant across the four application scenarios. This is because the primary difference among the four application scenarios is the distance from the keyboard to the receiver. Given the speed of electromagnetic wave propagation, an increase in the distance of several meters hardly impacts the latency of communication.

To further validate the robustness of the keyboard, we conducted a repetitive experiment. For each scenario depicted in

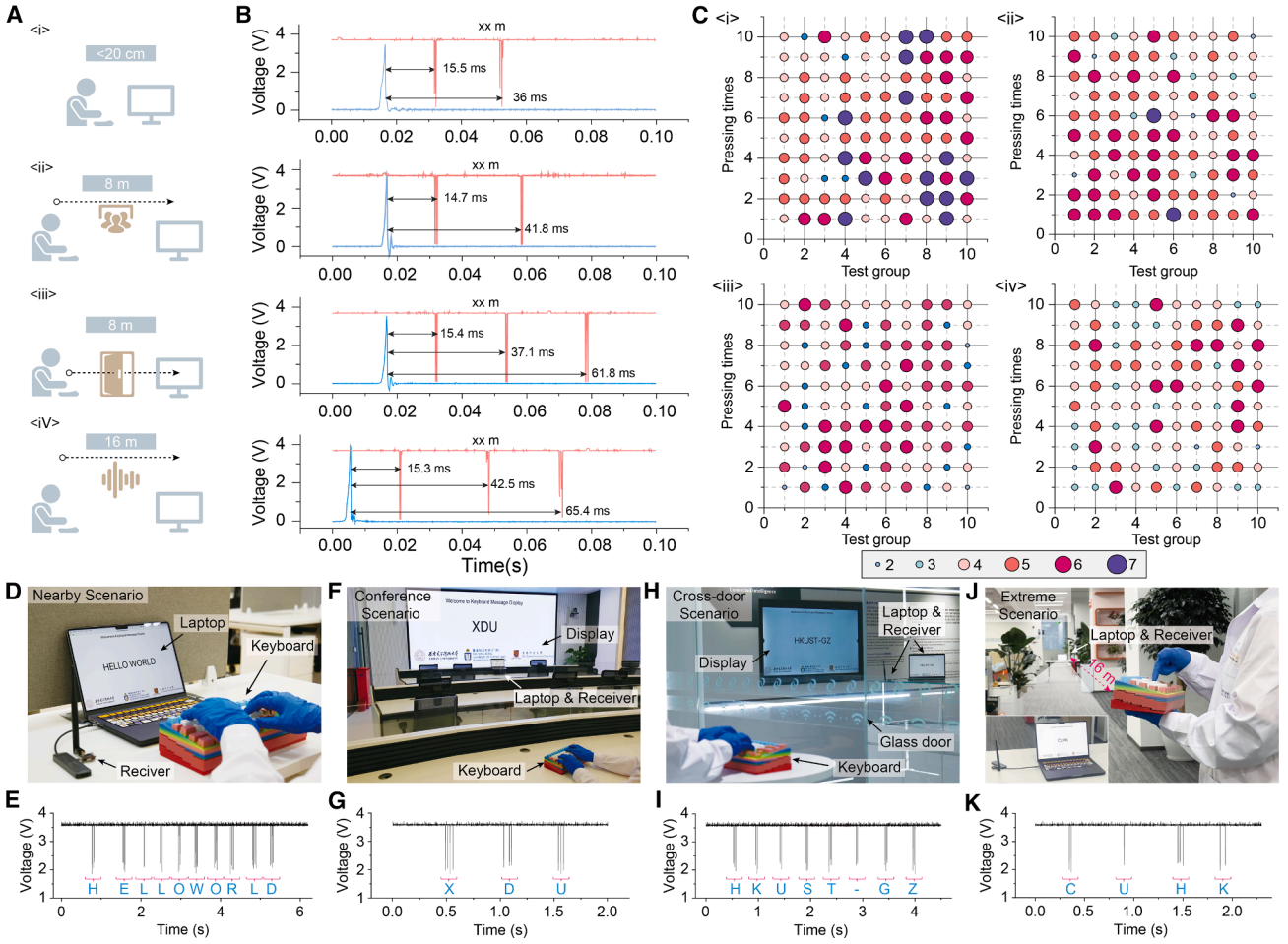

Figure 5. Application showcase of the battery-free wireless keyboard and its interactive quality assessment

(A) The tested scenarios, including (i) nearby scenario: normal working mode, (ii) far-distance scenario: theater mode, (iii) cross-door scenario: conference room mode, and (iv) noisy scenario: interference mode. The wireless keyboard is intentionally positioned at different distances from the receiver, either obstructed or unobstructed by barriers, to assess its communication range and latency.

(B) Illustration of the voltage produced by the key button and the signal recorded by the receiver within the same time frame to show communication latency. Despite the increased communication distance, the latency is controlled at around 15 ms, accounting for the first signal captured.

(C) Test results presented in heatmaps for the four designed scenarios. Each scenario consists of 10 independent groups, with each group containing 10 tests. Each circle represents an individual test, and the circle size and color indicate the number of packets received in the corresponding test: a larger circle size and darker color indicate higher numbers of packets transmitted.

(D) A real-world example of scenario (i).

(E) A real-world example of scenario (ii).

(F) A real-world example of scenario (iii).

(G) A real-world example of scenario (iv).

(H) The packet signal received in real-world scenario (i). The decoded information is “Hello World.”

(I) The packet signal received in real-world scenario (ii). The decoded information is “XDU.”

(J) The packet signal received in real-world scenario (iii). The decoded information is “HKUST(GZ).”

(K) The packet signal received in real-world scenario (iv). The decoded information is “CUHK.”

Figure 5A, we carried out 10 groups of tests, with each group comprising 10 individual tests. In other words, a total of 100 independent tests were conducted for each application scenario, and a total of 400 independent tests were conducted for the four application scenarios. The heatmaps with circles in Figure 5C present the test results. Each circle represents an individual test, with the size and color of the circle indicating the number of packets received during the corresponding test. Specifically, larger circles and darker colors signify a greater number of transmitted packets. Analysis of the 400 tests conducted across the four application scenarios reveals that there were no instances of unsuccessful transmission, with a minimum of two packets transmitted per individual keystroke. Figures 5D, 5F, 5H, and 5J present the four real-world scenarios in which we conducted the above tests. In these scenarios, we successfully typed “Hello World,” “XDU,” “HKUST(GZ),” and “CUHK” on the screen at the

receiver end using the battery-free wireless keyboard. Figures 5E, 5G, 5I, and 5K show the raw signals received in different scenarios. One can then accurately interpret the input commands transmitted from the keyboard by decoding the unique identifiers and differentiating packets associated with distinct keystrokes. Video S3 demonstrates how the keyboard functions in the context of the laboratory test.

DISCUSSION

By employing a cross-disciplinary design methodology, we have developed a truly battery-free wireless keyboard with all features for the first time. Thanks to the intricate engineering of a hysteresis mechanism and an instantaneous magnetic pole-swapping system, the compact and miniaturized harvester integrated into the keyboard is capable of efficiently capturing energy from subtle fingertip motion during keystrokes. The underlying principle was elucidated from a dynamic perspective, grounded in the analysis of the varying profiles of potential energy. A comprehensive assessment of the energy-harvesting performance was conducted, and the output characteristics, including voltage, current, and power, were determined. The robustness in terms of the power generation capability was evidenced by a test conducted with 20 participants, regardless of gender and user habits, revealing that the harvester could harness at least 45 μJ of energy from a single keystroke cycle. An auxiliary circuit was designed to achieve the desired functionality of the keyboard, establishing unidirectional communication with the computer for the transmission of input commands. Due to the simple yet reliable schematic and the choice of ultra-low-power circuit elements, the circuitry consumed only about 13.07 μJ for transmitting a single BLE packet. As a result, the combination of the well-designed energy harvester and the ultra-low functional circuit allows for the realization of a fully self-powered wireless keyboard that facilitates wireless interaction with computers. Finally, a thorough assessment comprising 400 tests in four application scenarios was conducted to examine the interactive performance of the keyboard. The results indicated a perfect success rate of 100%, a communication range exceeding 16 m, and a consistent latency of about 15 ms. While these results demonstrate the feasibility and robustness of our battery-free wireless keyboard, we recognize that further evaluations are essential to advance the system toward product-level maturity. In particular, user-dependent factors, such as typing speed and input frequency, may influence the harvester's voltage and current outputs, potentially affecting communication reliability. A more systematic investigation of these effects will be pursued in future work to enhance the adaptability and optimization of the system under diverse usage conditions.

METHODS

Quasi-static model

For an individual EMG, its total mechanical potential energy, U, is the sum of the elastic potential energy, U_e, from both the buffering spring and the restoring spring; the magnetic potential energy, U_m, between the magnet and the ferromagnetic core; and the potential energy, U_s, representing the stoppers that limit the upper and lower movements of the rotatable frame. The formula is given by

$$U(x,\theta) = U_e(x,\theta) + U_m(\theta) + U_s(\theta). \quad \text{(Equation 1)}$$

U is a function of two key geometric parameters, x (fingertip displacement) and θ (the angle of the rotatable frame), as shown in Figure 2B. The elastic potential energy can be expressed as

$$U_e(x,\theta) = \frac{1}{2}k_r(-\theta L_r + \theta_r L_r)^2 + \frac{1}{2}k_b[x' + (\theta L_b - \theta_s L_b)]^2, \quad \text{(Equation 2)}$$

where k_r represents the stiffness coefficient of the restoring spring; θ_r denotes the angle of the rotatable frame when the restoring spring is at its natural length without the ferromagnetic core; L_r signifies the distance from the force application point of the restoring spring to the rotation center, which is annotated in Figure 2B; k_b stands for the stiffness coefficient of the buffering spring; x' indicates the position of the upper end of the buffering spring, i.e., the displacement of the keycap; θ_s refers to the angle of the rotatable frame when it is at the upper limited position; and L_b measures the distance from the force application point of the buffering spring to the rotation center.

Although the fingertip applies the external force to the keycap of the EMG unit, it is necessary to distinguish between x and x'. For instance, when k_b tends to infinity and the rotatable frame is pushed down from the upper stopper position, it can be considered that the external force directly pushes the rotatable frame and the magnet. When the rotatable frame is pushed past the operation position where $\theta = 0$, the force from the ferromagnetic core on the magnet is downward, causing the rotatable frame to switch instantly to the lower stopper position. If the fingertip's speed is slow, the fingertip will then detach from the keycap. Therefore, x' is expressed as

$$x' = \begin{cases} x + 2\theta_s L_b & \text{if } x + 2\theta_s L_b < -(\theta - \theta_s)L_b \\ x & \text{if } x > -(\theta - \theta_s)L_b \\ -(\theta - \theta_s)L_b & \text{others} \end{cases}. \quad \text{(Equation 3)}$$

As the rotatable frame rotates between the upper and lower limited positions, the magnetic interaction between the magnet and the ferromagnetic core can be considered a nonlinear spring with negative stiffness, expressed as

$$U_m(\theta) = \frac{1}{2}k_1(\theta L)^2 + \frac{1}{4}k_3(\theta L)^4, \quad \text{(Equation 4)}$$

where k_1 and k_3 are two constants used to fit the actual nonlinear magnetic force using the Duffing-type model, as illustrated in Figure 2B, and L is the equivalent lever arm of the magnetic force. The stopper, formed by the ferromagnetic core and magnetic conductors, can be modeled as a spring with a large stiffness coefficient to represent its limiting effect, expressed as

$$U_s(\theta) = \frac{1}{2}k_s(\theta L - \theta_s L)^2\langle \theta L - \theta_s L > 0\rangle + \frac{1}{2}k_s(\theta L + \theta_s L)^2\langle \theta L + \theta_s L < 0\rangle, \quad \text{(Equation 5)}$$

where k_s is the equivalent stiffness coefficient of the stopper and $\langle\cdot\rangle$ is the Heaviside unit step function.

Dynamic model

The rotatable frame is the only mobile part of the EMG unit, and the governing equation of its angle can be derived using the Lagrange equation, i.e.,

$$\frac{d}{dt}\left(\frac{\partial[T(\theta) - U(x,\theta)]}{\partial\dot{\theta}}\right) - \frac{\partial[T(\theta) - U(x,\theta)]}{\partial\theta} = -c_s\dot{\theta}\langle\theta > \theta_s\rangle - c_s\dot{\theta}\langle\theta > \theta_s\rangle, \quad \text{(Equation 6)}$$

where c_s represents the damping coefficient that causes energy dissipation during the stopper collision and $T(\theta)$ is the kinetic energy function of the rotatable frame, expressed as

$$T(\theta) = \frac{1}{2}J\dot{\theta}^2, \quad \text{(Equation 7)}$$

where J is the moment of inertia of the rotatable frame. Therefore, the relationship between the angle of the rotatable frame and the displacement of the fingertip can be expressed as

$$J\ddot{\theta} + k_rL_r^2(\theta - \theta_r) + k_bL_b[x' + L_b(\theta - \theta_s)] + k_1\theta L^2 + k_3\theta^3L^4 + k_sL^2(\theta - \theta_s)\langle\theta > \theta_s\rangle + k_sL^2(\theta + \theta_s)\langle\theta < -\theta_s\rangle - c_s\dot{\theta}\langle\theta > \theta_s\rangle - c_s\dot{\theta}\langle\theta < -\theta_s\rangle = 0. \quad \text{(Equation 8)}$$

The simulation results presented in the supplemental information (Figures S3–S9) are obtained using the above models.

Building on Equations 1, 2, 3, 4, 5, 6, 7, and 8, the electromagnetic output follows $V \approx N\cdot d\Phi/dt$, where the magnetic flux Φ is set by the magnetic circuit reluctance (core geometry/material and the magnet-core air gap). Coupling this with the quasi-static energy landscape and the rotational dynamics yields clear design trends: increasing coil turns N raises the induced voltage but also the coil resistance, so the harvested energy is maximized when the external load approximately matches the coil resistance; enlarging the core cross-section or using higher-permeability materials lowers reluctance and increases Φ until approaching magnetic saturation; and reducing the magnet-core air gap strongly increases Φ and energy per keystroke but tightens mechanical tolerances. The implemented dimensions and coil specification follow these model-derived rules and are summarized in Figure S12.

Prototyping and measurement

The primary components of the battery-free keyboard, including the keycaps, the substrate, and the keyboard housing, were produced using 3D printers (model: FUNMAT PRO and Bambu Lab X1E). The ferromagnetic bar was machined by cutting, while the coils were handcrafted using a winding machine (model: QGSD-Automatic). Neodymium N52-grade magnets were used to achieve a high energy-harvesting efficiency. The buffering and restoring springs were standard items purchased from suppliers. The PCB was designed using the software Altium Designer and then sent out for fabrication by an external supplier. We provided the supplier with detailed specifications, including the etching of copper pathways, drilling for component placements, and soldering of the electronic components. A 4-channel oscilloscope (RIGOL HDO 1140, 100 MHz bandwidth) was used to measure the voltage outputs in the experiment, and a power analyzer (model: OTII-ARC-001) was utilized to measure the current. A force gauge (model HANDPI SH-30N, Figure S11) was employed to assess the fingertip force applied to the keycaps during tests. The data-processing algorithm was written in Python and implemented on a MacBook Pro laptop to interpret the packets transmitted from the keyboard.

RESOURCE AVAILABILITY

Lead contact

Requests for further information and resources should be directed to and will be fulfilled by the lead contact, Wei-Hsin Liao (whliao@cuhk.edu.hk).

Materials availability

This study did not generate new, unique materials.

Data and code availability

- No code was generated in this study.
- The source data of this study can be found in the supplemental information.
- For any further inquiries or requests for information, please contact the lead corresponding author.

ACKNOWLEDGMENTS

This work was financially supported by the Guangdong Basic and Applied Basic Research Foundation (grant no. 2025A1515011342), the National Natural Science Foundation of China (grant no. 52305135), the Hong Kong Research Grants Council (project no. CUHK14211823), and The Chinese University of Hong Kong (project IDs 3134164 and 4055178).

AUTHOR CONTRIBUTIONS

X.L., G.H., and W.-H.L. conceived the idea, supervised the project, and secured the funding. X.L. and G.H. oversaw the data post-processing, guided figure preparation, and drafted the manuscript. X.C. and Y.L. prepared the prototype. Y.L. built the CAD model. X.C. designed the experiment, conducted the test, collected the data, and prepared the figures. Under the supervision of X.L. and G.H., Y.W. further polished the figures, and Y.Z. helped with figure rendering and photographing. W.-H.L. polished the manuscript. Q.L., D.Z., and C.W. engaged in the discussions.

DECLARATION OF INTERESTS

X.L. and W.-H.L. have a PCT patent application related to this work (application number: PCT/CN2025/072201).

SUPPLEMENTAL INFORMATION

Supplemental information can be found online at https://doi.org/10.1016/j.xcrp.2025.102972.

Received: May 29, 2025
Revised: September 11, 2025
Accepted: October 26, 2025
Published: November 21, 2025

REFERENCES

1. Greenbaum, D., and Gerstein, M. (2015). The innovators how a group of hackers, geniuses, and geeks created the digital revolution. Science *347*, 956.

2. Lieberman, H. (2007). From whole earth to the whole web. Science *315*, 1369.

3. Wang, Z.L. (2013). Triboelectric nanogenerators as new energy technology for self-powered systems and as active mechanical and chemical sensors. ACS Nano *7*, 9533–9557.

4. Karnan, M., Akila, M., and Krishnaraj, N. (2011). Biometric personal authentication using keystroke dynamics: a review. Appl. Soft Comput. *11*, 1565–1573.

5. Xia, K., Wu, D., Fu, J., Hoque, N.A., Ye, Y., and Xu, Z. (2020). Tunable output performance of triboelectric nanogenerator based on alginate metal complex for sustainable operation of intelligent keyboard sensing system. Nano Energy *78*, 105263.

6. Lin, S., Zhu, J., Yu, W., Wang, B., Sabet, K.A., Zhao, Y., Cheng, X., Hojaiji, H., Lin, H., Tan, J., et al. (2022). A touch-based multimodal and cryptographic bio-human–machine interface. Proc. Natl. Acad. Sci. USA *119*, e2201937119.

7. Blossey, R. (2003). Self-cleaning surfaces—virtual realities. Nat. Mater. *2*, 301–306.

8. Liu, Z., Li, T., Li, S., and Mi, C.C. (2024). Advancements and challenges in wireless power transfer: a comprehensive review. Nexus *1*, 100014.

9. Sezer, N., and Koç, M. (2021). A comprehensive review on the state-of-the-art of piezoelectric energy harvesting. Nano Energy *80*, 105567.

10. Maharjan, P., Bhatta, T., Cho, H., Hui, X., Park, C., Yoon, S., Salauddin, M., Rahman, M.T., Rana, S.S., and Park, J.Y. (2020). A fully functional universal self-chargeable power module for portable/wearable electronics and self-powered IoT applications. Adv. Energy Mater. *10*, 2002782.

11. Zhang, Y., Castro, D.C., Han, Y., Wu, Y., Guo, H., Weng, Z., Xue, Y., Ausra, J., Wang, X., Li, R., et al. (2019). Battery-free, lightweight, injectable microsystem for in vivo wireless pharmacology and optogenetics. Proc. Natl. Acad. Sci. USA *116*, 21427–21437.

12. Afzal, S.S., Akbar, W., Rodriguez, O., Doumet, M., Ha, U., Ghaffarivardavagh, R., and Adib, F. (2022). Battery-free wireless imaging of underwater environments. Nat. Commun. *13*, 5546.

13. Su, L., Kuang, S., Zhao, Y., Li, J., Zhao, G., Wang, Z.L., and Zi, Y. (2024). Self-powered visualized tactile-acoustic sensor for accurate artificial perception with high brightness and record-low detection limit. Sci. Adv. *10*, eadq8989.

14. Wang, Y., Du, H., Yang, H., Xi, Z., Zhao, C., Qian, Z., Chuai, X., Peng, X., Yu, H., Zhang, Y., et al. (2024). A rolling-mode triboelectric nanogenerator with multi-tunnel grating electrodes and opposite-charge-enhancement for wave energy harvesting. Nat. Commun. *15*, 6834.

15. Ba, K., Liu, G., Ma, G., Chen, C., Pu, L., He, X., Chen, X., Wang, Y., Zhu, Q., Wang, D., et al. (2024). Bionic perception and transmission neural device based on a self-powered concept. Cell Rep. Phys. Sci. *5*, 102048.

16. Wang, J., Li, S., Yi, F., Zi, Y., Lin, J., Wang, X., Xu, Y., and Wang, Z.L. (2016). Sustainably powering wearable electronics solely by biomechanical energy. Nat. Commun. *7*, 12744.

17. Donelan, J.M., Li, Q., Naing, V., Hoffer, J.A., Weber, D.J., and Kuo, A.D. (2008). Biomechanical energy harvesting: generating electricity during walking with minimal user effort. Science *319*, 807–810.

18. Petritz, A., Karner-Petritz, E., Uemura, T., Schäffner, P., Araki, T., Stadlober, B., and Sekitani, T. (2021). Imperceptible energy harvesting device and biomedical sensor based on ultraflexible ferroelectric transducers and organic diodes. Nat. Commun. *12*, 2399.

19. Zou, Y., Raveendran, V., and Chen, J. (2020). Wearable triboelectric nanogenerators for biomechanical energy harvesting. Nano Energy *77*, 105303.

20. Shveda, R.A., Rajappan, A., Yap, T.F., Liu, Z., Bell, M.D., Jumet, B., Sanchez, V., and Preston, D.J. (2022). A wearable textile-based pneumatic energy harvesting system for assistive robotics. Sci. Adv. *8*, eabo2418.

21. Cao, Y., Fan, S., Tang, Y., Shan, Q., Gao, C., Sepúlveda, N., Hou, D., and Zhang, G. (2024). Human-motion adaptability enhancement of wearable electromagnetic vibration energy harvesters toward self-sustained body sensor networks. Cell Rep. Phys. Sci. *5*, 102117.

22. Lai, Z., Xu, J., Bowen, C.R., and Zhou, S. (2022). Self-powered and self-sensing devices based on human motion. Joule *6*, 1501–1565.

23. De Pasquale, G., Kim, S.-G., and De Pasquale, D. (2015). GoldFinger: wireless human–machine interface with dedicated software and biomechanical energy harvesting system. IEEE/ASME Transactions On Mechatronics *21*, 565–575.

24. Zhu, M., Sun, Z., Zhang, Z., Shi, Q., He, T., Liu, H., Chen, T., and Lee, C. (2020). Haptic-feedback smart glove as a creative human-machine interface (HMI) for virtual/augmented reality applications. Sci. Adv. *6*, eaaz8693.

25. Zhang, T., Liang, H., Wang, Z., Qiu, C., Peng, Y.B., Zhu, X., Li, J., Ge, X., Xu, J., Huang, X., et al. (2022). Piezoelectric ultrasound energy–harvesting device for deep brain stimulation and analgesia applications. Sci. Adv. *8*, eabk0159.

26. Hu, Y., Parida, K., Zhang, H., Wang, X., Li, Y., Zhou, X., Morris, S.A., Liew, W.H., Wang, H., Li, T., et al. (2022). Bond engineering of molecular ferroelectrics renders soft and high-performance piezoelectric energy harvesting materials. Nat. Commun. *13*, 5607.

27. Yang, Z., Zhou, S., Zu, J., and Inman, D. (2018). High-performance piezoelectric energy harvesters and their applications. Joule *2*, 642–697.

28. Godard, N., Allirol, L., Latour, A., Glinsek, S., Gérard, M., Polesel, J., Domingues Dos Santos, F., and Defay, E. (2020). 1-mW vibration energy harvester based on a cantilever with printed polymer multilayers. Cell Rep. Phys. Sci. *1*, 100068.

29. Kang, W., and Huber, J.E. (2022). Energy harvesting based on compressive stress-induced ferroelectric/ferroelastic switching in polycrystalline ferroelectric materials. Cell Rep. Phys. Sci. *3*, 100707.

30. Chen, J., Zhu, G., Yang, J., Jing, Q., Bai, P., Yang, W., Qi, X., Su, Y., and Wang, Z.L. (2015). Personalized keystroke dynamics for self-powered human–machine interfacing. ACS Nano *9*, 105–116.

31. Li, S., Peng, W., Wang, J., Lin, L., Zi, Y., Zhang, G., and Wang, Z.L. (2016). All-elastomer-based triboelectric nanogenerator as a keyboard cover to harvest typing energy. ACS Nano *10*, 7973–7981.

32. Wu, C., Ding, W., Liu, R., Wang, J., Wang, A.C., Wang, J., Li, S., Zi, Y., and Wang, Z.L. (2018). Keystroke dynamics enabled authentication and identification using triboelectric nanogenerator array. Mater. Today *21*, 216–222.

33. Jeon, S.-B., Park, S.-J., Kim, W.-G., Tcho, I.-W., Jin, I.-K., Han, J.-K., Kim, D., and Choi, Y.-K. (2018). Self-powered wearable keyboard with fabric based triboelectric nanogenerator. Nano Energy *53*, 596–603.

34. Yi, J., Dong, K., Shen, S., Jiang, Y., Peng, X., Ye, C., and Wang, Z.L. (2021). Fully fabric-based triboelectric nanogenerators as self-powered human–machine interactive keyboards. Nano-Micro Lett. *13*, 103–113.

35. Yin, W., Xie, Y., Long, J., Zhao, P., Chen, J., Luo, J., Wang, X., and Dong, S. (2018). A self-power-transmission and non-contact-reception keyboard based on a novel resonant triboelectric nanogenerator (R-TENG). Nano Energy *50*, 16–24.

36. Hong, H., Chen, T., Yang, J., Hu, Y., Hu, J., Li, D., Liu, F., Liu, L., and Wu, H. (2024). Omnidirectional water wave energy harvesting by a spherical triboelectric nanogenerator with sliced-pizza-shaped electrodes. Cell Rep. Phys. Sci. *5*, 101933.

37. Wacharasindhu, T., and Kwon, J.W. (2008). A micromachined energy harvester from a keyboard using combined electromagnetic and piezoelectric conversion. J. Micromech. Microeng. *18*, 104016.

38. Wang, P., Liu, R., Ding, W., Zhang, P., Pan, L., Dai, G., Zou, H., Dong, K., Xu, C., and Wang, Z.L. (2018). Complementary electromagnetic-triboelectric active sensor for detecting multiple mechanical triggering. Adv. Funct. Mater. *28*, 1705808.

39. Maharjan, P., Bhatta, T., Park, C., Cho, H., Shrestha, K., Lee, S., Salauddin, M., Rahman, M., Rana, S.S., and Park, J.Y. (2021). High-performance keyboard typing motion driven hybrid nanogenerator. Nano Energy *88*, 106232.

40. Bai, Y.-W., and Yang, M.-Y. (2008). An improved design of a wireless keyboard powered by solar cells and a large capacitor. IEEE Trans. Consumer Electron. *54*, 1355–1359.

41. Zada, M., Iman, U.R., Basir, A., and Yoo, H. (2024). Battery-free digitally embroidered smart textile energy harvester for wearable healthcare IoTs. IEEE Trans. Ind. Electron. *71*, 9865–9874.

42. Cai, Z., Chen, Q., Shi, T., Zhu, T., Chen, K., and Li, Y. (2023). Battery-free wireless sensor networks: a comprehensive survey. IEEE Internet Things J. *10*, 5543–5570.

43. Liu, S., Xu, X., and Claypool, M. (2022). A survey and taxonomy of latency compensation techniques for network computer games. ACM Comput. Surv. *54*, 1–34.